Nonlinear Dynamics and Chaos in the Sea and Land Breeze

YIZHAK FELIKS

Department of Mathematics, Israel Institute for Biological Research, Ness-Ziona, Israel

(Manuscript received 28 April 2003, in final form 24 February 2004)

ABSTRACT

In this work the evolution of the sea and land breeze is studied using a nonlinear model under calm synoptic conditions and diurnal periodic forcing of ground temperature. The breeze is examined as a function of the strength of the heating amplitude of ground temperature θ_0. For $\theta_0 \leq 6$°C, the solution is quasi-periodic with two incommensurate oscillations of 24 and 22.6 h; the last is the inertial oscillation at latitude 32°N. A very low frequency oscillation (VLFO) of 16 days, which is the linear combination of the two incommensurate oscillations, is also obtained. For $\theta_0 = 7$°C, the solution becomes nonperiodic. For $\theta_0 \geq 10$°C, chaotic solutions are obtained. In the chaotic regime the prominent oscillations can be divided into two classes. One class includes short-time-scale oscillations, such as the 24-h oscillation, the 22.4-h slightly modified inertial oscillation, and their harmonics. The second class incorporates time scales that are larger than a week, such as 15 days, which is a linear combination of the 24- and 22.4-h oscillations. The flow in the second class is in geostrophic balance. The kinetic energy, which manifests spells of very large energy fluctuations, is examined. During these spells the amplitude of the VLFO is large, and the amplitude of the 24-h oscillation is small compared to the spells where the fluctuations in the kinetic energy are small.

Analyses of the wind observations in the central coast of Israel in the summer months show great similarity to the model simulation in the chaotic regime. A VLFO of 10 days, which is prominent in its parallel to the shore component, is interpreted to be the result of the nonlinear interaction between the inertial oscillation at the central latitude of the eastern Mediterranean, 33.5°N, and the 24-h oscillation as obtained in the present model.

1. Introduction

The sea and land breeze has been extensively studied by observations, and analytical and numerical models (see, e.g., Atkinson 1989), so the physics of the breeze is quite well understood. It is widely believed that the asymptotic behavior of the breeze, under persistent synoptic conditions and periodic forcing of the heating and cooling, is periodic with the period of the forcing, 24 h. This is the reason for the short integration period—several hours up to 3 days—examined by the numerical models. Dalu and Pielke (1989) utilized a linear model in order to examine the time it takes for the asymptotic periodic behavior to be reached starting from given initial conditions. The characteristic time scale suggested by them is given by $T = (f^2 + \lambda^2)^{-1/2}$, where λ^{-1} is the damping time due to friction and f is the inertial frequency. This characteristic time is equal to several hours, given the value used in their paper for friction. Nonperiodic asymptotic behavior of the breeze was ultimately considered to be due to changes in synoptic conditions or due to aperiodic forcing such as ground temperature.

Corresponding author address: Y. Feliks, Dept. of Mathematics, Israel Institute for Biological Research, P.O.B. 19 Ness-Ziona, Israel. E-mail: feliks@iibr.gov.il

The clockwise rotation of the breeze in the Northern Hemisphere is due to the Coriolis force; its rate depends on latitude and friction as shown first by Haurwitz (1947). More extensive studies of the role of the different physical factors in the rotation and its rate were performed by Neumann (1977), Kusuda and Alpert (1983), and Alpert et al. (1984). In the linear models of the breeze no inertial oscillation is obtained, and only the diurnal oscillation exists in the attractor of the solution. In nonlinear studies of the breeze, there is a study of neither the attractor of the breeze nor the different oscillations such as the inertial oscillation due to Coriolis force, and their spatial structure in different phases.

Numerical models studied extensively the role of the nonlinear terms in sea-breeze circulation. The most prominent consequences of the nonlinear terms are the inland propagation of the sea breeze and its front, which was first studied numerically by Estoque (1961), Pearson (1973), Neumann and Mahrer (1974), Lambert (1974), Physik (1976), and analytically by Feliks (1988, 2000) and others.

In this study we examine the asymptotic behavior of the breeze under calm synoptic conditions and periodic forcing of the ground temperature by utilizing a nonlinear model. We show that the attractor of the breeze can be periodic, quasi-periodic, or chaotic (i.e., strange

attractor) as a function of amplitude of the ground temperature. We study the robust skeleton of the attractor (Ghil et al. 2002) and show the spatial structure of the prominent oscillations, such as the inertial oscillation and the diurnal oscillation. Also we find very long oscillations with periods larger than 10 days.

2. The model

In this paper, we focus on circulations in the lower atmosphere; hence, their heights are much smaller than the scale height of the atmosphere. This allows us to use the Boussinesq incompressible approximation of the equations of motion. We utilize a two-dimensional numerical model of Feliks (1993) to study the sea and land breeze in a vertical cross section perpendicular to the sea shore, where $x < 0$ is the sea and $x > 0$ is the land. We did some modification in the numerical schemes particularly in the horizontal advection terms.

a. Model equations

The horizontal components of the equations of motion are

$$\frac{\partial u}{\partial t} = -u\frac{\partial u}{\partial x} - w\frac{\partial u}{\partial z} + fv - \frac{1}{\rho_m}\frac{\partial p}{\partial x} + \frac{\partial}{\partial z}\left(K_m\frac{\partial u}{\partial z}\right) + K_H\frac{\partial^2 u}{\partial x^2} - g\frac{\partial h}{\partial x}, \tag{1}$$

$$\frac{\partial v}{\partial t} = -u\frac{\partial v}{\partial x} - w\frac{\partial v}{\partial z} - fu - \frac{1}{\rho_m}\frac{\partial p}{\partial y} + \frac{\partial}{\partial z}\left(K_m\frac{\partial v}{\partial z}\right) + K_H\frac{\partial^2 v}{\partial x^2}, \tag{2}$$

where ρ_m is the mean air density and h is the height of the material surface. The third component of the equation of motion is replaced by the hydrostatic approximation:

$$\frac{1}{\rho_m}\frac{\partial p}{\partial z} = -\frac{\rho' g}{\rho_m}, \tag{3}$$

where ρ' is the perturbation density so that $\rho = \rho_m + \rho'$.

The incompressible continuity equation is

$$\frac{\partial u}{\partial x} + \frac{\partial w}{\partial z} = 0. \tag{4}$$

The thermodynamic energy equation is written in terms of potential temperature:

$$\frac{\partial \theta}{\partial t} = -u\frac{\partial \theta}{\partial x} - w\frac{\partial \theta}{\partial z} + \frac{\partial}{\partial z}\left(K_e\frac{\partial \theta}{\partial z}\right) + K_H\frac{\partial^2 \theta}{\partial x^2}. \tag{5}$$

The equation of state is

$$-\frac{g\rho'}{\rho_m} = \frac{g\theta'}{\theta_m}, \tag{6}$$

where θ_m is the mean potential temperature and θ' is the perturbation potential temperature so that $\theta = \theta_m + \theta'$.

b. Exchange coefficients

The closure of the model equations requires an explicit formulation of the exchange coefficients in terms of the dependent variables. The formulation adopted follows Pandolfo and Jacobes (1973), and Huss and Feliks (1981). We assume four stability regimes, which are identified by the local Richardson number; that is,

$$\mathrm{Ri} = \frac{\dfrac{g}{\theta}\dfrac{\partial \theta}{\partial z}}{\left|\dfrac{\partial(u, v)}{\partial z}\right|^2}. \tag{7}$$

We have adopted the concept of mixing length, without insisting on its physical content:

$$l = k(z + z_0)\left[1 + 4\left(\frac{z + z_0}{z_m}\right)\right]^{-1}, \tag{8}$$

where z_m is the altitude at which 1 attains its maximum. According to an observational study by Lettau (1962), we chose $z_m = 250$ m. The roughness length is $z_0 = 2$ cm.

The exchange coefficients in the four regimes are

$$\mathrm{Ri} > \frac{1}{|\alpha|}\colon K_e = K_m = 0.1\ \mathrm{m^2\ s^{-1}}, \tag{9a}$$

$$0 \le \mathrm{Ri} \le \frac{1}{|\alpha|}\colon K_m = K_e = l^2(1 + \alpha\mathrm{Ri})^2\left|\frac{\partial(u, v)}{\partial z}\right|, \tag{9b}$$

$$\mathrm{Ri}_c \le \mathrm{Ri} \le 0\colon K_m = l^2(1 - \alpha\mathrm{Ri})^{-2}\left|\frac{\partial(u, v)}{\partial z}\right|,$$

$$K_e = K_m(1 - \alpha\mathrm{Ri})^{-1}, \tag{10}$$

$$\mathrm{Ri} \le \mathrm{Ri}_c\colon K_e = \frac{l^2}{k^2}h\left|\frac{g}{\theta}\frac{\partial \theta}{\partial z}\right|^{1/2},$$

$$K_m = A|\mathrm{Ri}|^{-1/6}K_e, \tag{11}$$

where $h = 0.9$ is Priestley's heat convection constant, $k = 0.4$ is the von Kármán constant, $\alpha = -0.3$, $A = 0.56$, and $\mathrm{Ri}_c = -0.04$. The minimum value of the vertical exchange coefficients is 0.1 $\mathrm{m^2\ s^{-1}}$.

c. Boundary and initial conditions

The wind components u, v, and w vanish at the sea and land surface. At the upper boundary, u and v are taken to be equal to the specified geostrophic wind, which was taken as zero in this paper. The upper boundary is assumed to be a rigid lid; that is, $w = 0$. At the

upper boundary, θ is held constant and p is determined by the geostrophic wind; that is, $(1/\rho_m)(\partial p/\partial x) + g(\partial h/\partial x) = fv_g$. An equation for the material surface height h is found from the rigid lid assumption, Eqs. (1) and (4) as follows: derivative Eq. (1) by x and integrating it from the surface to the upper boundary, we get

$$\frac{\partial}{\partial t}\int_0^H \frac{\partial u}{\partial x}\,dz = 0 = \int_0^H \frac{\partial A}{\partial x}\,dz - gH\frac{\partial^2 h}{\partial x^2}, \quad (12)$$

where H is the height of the integration domain and A is the right-hand side of Eq. (1) without the h tendency term.

The ground temperature varies periodically with time to simulate the diurnal cycle of heating and cooling of the ground:

$$\theta = \begin{cases} 300\text{ K} + \theta_0 \sin(\omega t), & x > 0 \quad \text{(land)} \\ 300\text{ K}, & x < 0 \quad \text{(sea)}, \end{cases}$$
$$\omega = \frac{2\pi}{24\text{ h}}, \quad (13)$$

where $t = 0$ is sunrise.

At the lateral boundaries the derivative in the direction of the normal to the boundary was equal to zero.

In the following numerical simulations the initial condition of horizontal homogeneity was assumed.

d. Numerical aspects

The equations are applied to a grid contained within a vertical plane extending in the x coordinate perpendicular to the coastline. A staggered grid is used in the horizontal coordinate. The u, v components are computed on the grid points, while θ, p, and w are computed on the staggered grid points. The horizontal grid interval was taken as $\Delta x = 5$ km and 132 grid points were utilized: 66 points over the sea and 66 over the land, that is 320 km over the sea and 320 km over the land; 19 levels are taken at heights of 0, 0.62, 1.25, 2.5, 5, 10, 20, 40, 80, 160, 320, 640, 960, 1600, 2240, 2880, 3520, 4160, 4800, and 5440 m. A forward time scheme is used to approximate the time derivative. The ''component by component splitting method'' is used to solve the prognostic equations (Marchuk 1975). Horizontal advection terms are approximated by the four-point upwind scheme as suggested by Fletcher (1991, p. 297), and the diffusion is solved explicitly. Vertical diffusion and advection are solved implicitly to allow large time steps. Note that u, v, w, θ, and p are computed at the 20 levels, while K_m, K_e, and Ri are computed at midlevels. The time interval was $\Delta t = 90$ s. The properties of the numerical solution below, like the structure of the strange attractor and the transition to chaos, as function of the physical parameters, are sensitive to the time step used. For $\Delta t = 45$, 90 s the results were the same, but for $\Delta t = 180$ s the results were different, although the numerical solution is stable and smooth. In section 3 we study the structure of the attractor (as shown in Fig. 11). For $dt = 180$ s, this attractor is different. For $\theta_0 = 6$°C, the solution is not confined to the thin ring, and so one can think the solution is nonperiodic for $\theta_0 \geq 6$°C. In the physical space the snapshots of the circulation are very similar for $dt = 90$ or 180 s. We assume that in the larger time step the solution is more noisy, resulting in a less stable attractor.

TABLE 1. Physical and model parameters.

K_H	2×10^3 m^2 s^{-1}
f	14.585×10^{-5} sin ϕ/s
ϕ	32°N
Δx	5×10^3 m
Δt	90 s
ρ_m	1 kg m^{-3}
θ_m	300 K

The properties of the solution do not change as the domain size decreases by 100 km or increases by 100 km, but for much smaller domain of 320 km some properties of the solution change, particularly the periods of the very low frequency oscillation (VLFO). Increasing or decreasing the height of the domain by 1000 m does not change the properties of the solution, but for much shallower domain, such as 3540 m, the properties of the solution change, particularly the structure of the attractor $\theta_0 \leq 10$°C.

3. Results

In the basic experiment the model was integrated with the amplitude of the forcing $\theta_0 = 14$°C, and the rest of the parameters are listed in Table 1. Similar and larger values of the forcing amplitude were used in many studies of the sea and land breeze, such as Estoque (1961), Neumann and Mahrer (1971), Alpert et al. (1982), Feliks (1993), and others. The model was integrated for 1250 days, and only the last 650 days were analyzed in order to make sure transient response to the initial condition was forgotten owing to the damping of the motion, and that the solution is already in its attractor. In Figs. 1 and 2 the diurnal cycle of the breeze at days 641 and 866 is shown. Hour 0h is the time when surface temperature over the sea and land is uniform. This hour approximately corresponds to 0600 local time (LT) in the summer in the eastern Mediterranean. The diurnal cycle near the coast at the lower layers in these 2 days is similar. During daytime, 6h–12h, the sea breeze develops in the lower layers near the coast and propagates inland and into the sea, and expands to the upper layers. Later, at 15h–18h, the sea breeze near the coast weakens, but its inland propagation continues. The inland propagation is characterized by the sea-breeze front. The wind rotates in the clockwise direction due to Coriolis force. In the upper layers and away from the coast the flow in these 2 days differs significantly. The sea breeze

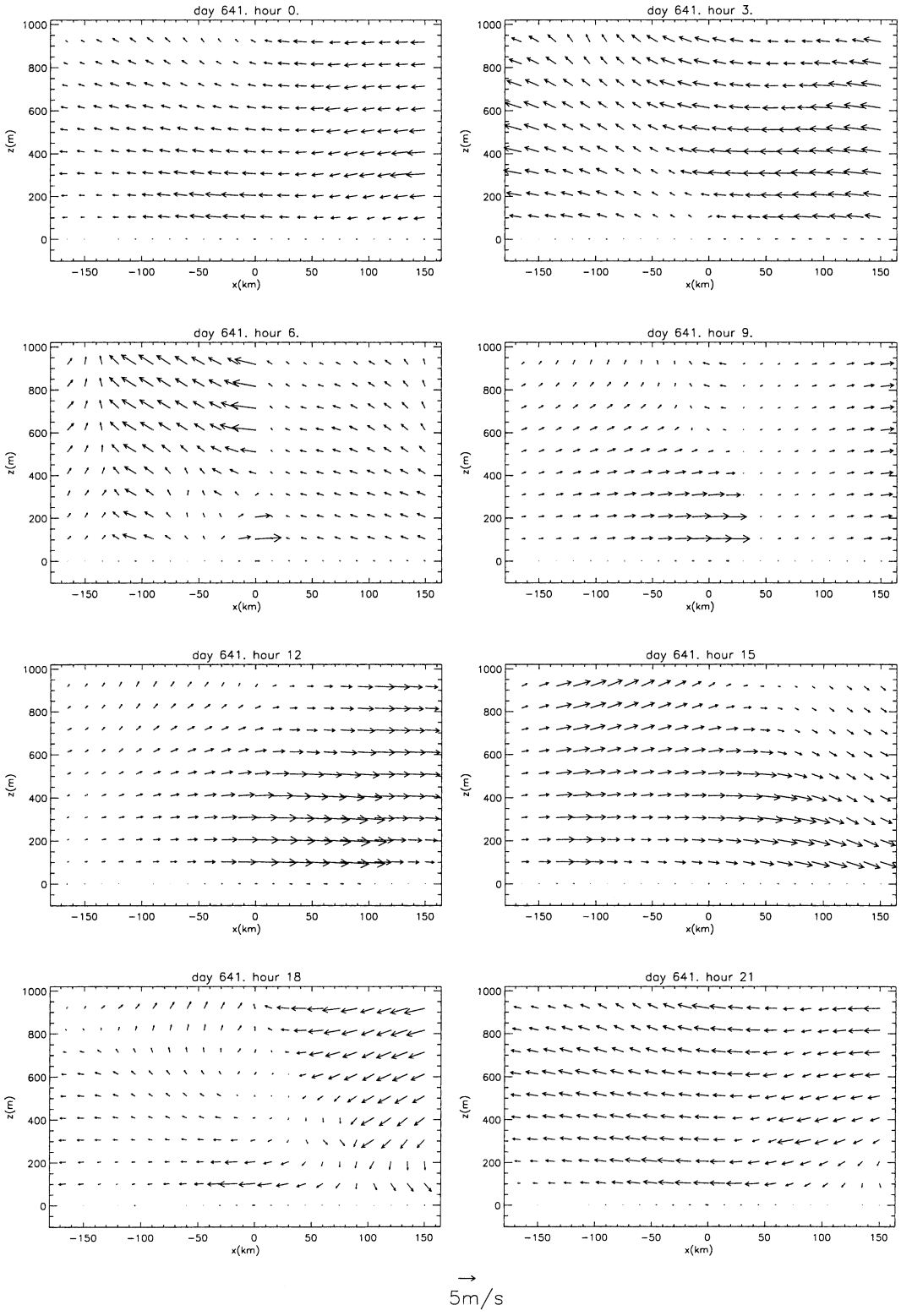

FIG. 1. Horizontal winds (m s^{-1}, arrows) at day 641 in a partial domain (between −150 km to sea and 150 km inland). Hour 0h corresponds to 0600 LT, $x < 0$ is sea, and $x > 0$ is land. The tail of the arrows corresponds to position in the x–z plane. An arrow pointing down indicates a wind from the north; an arrow pointing right indicates winds from the west.

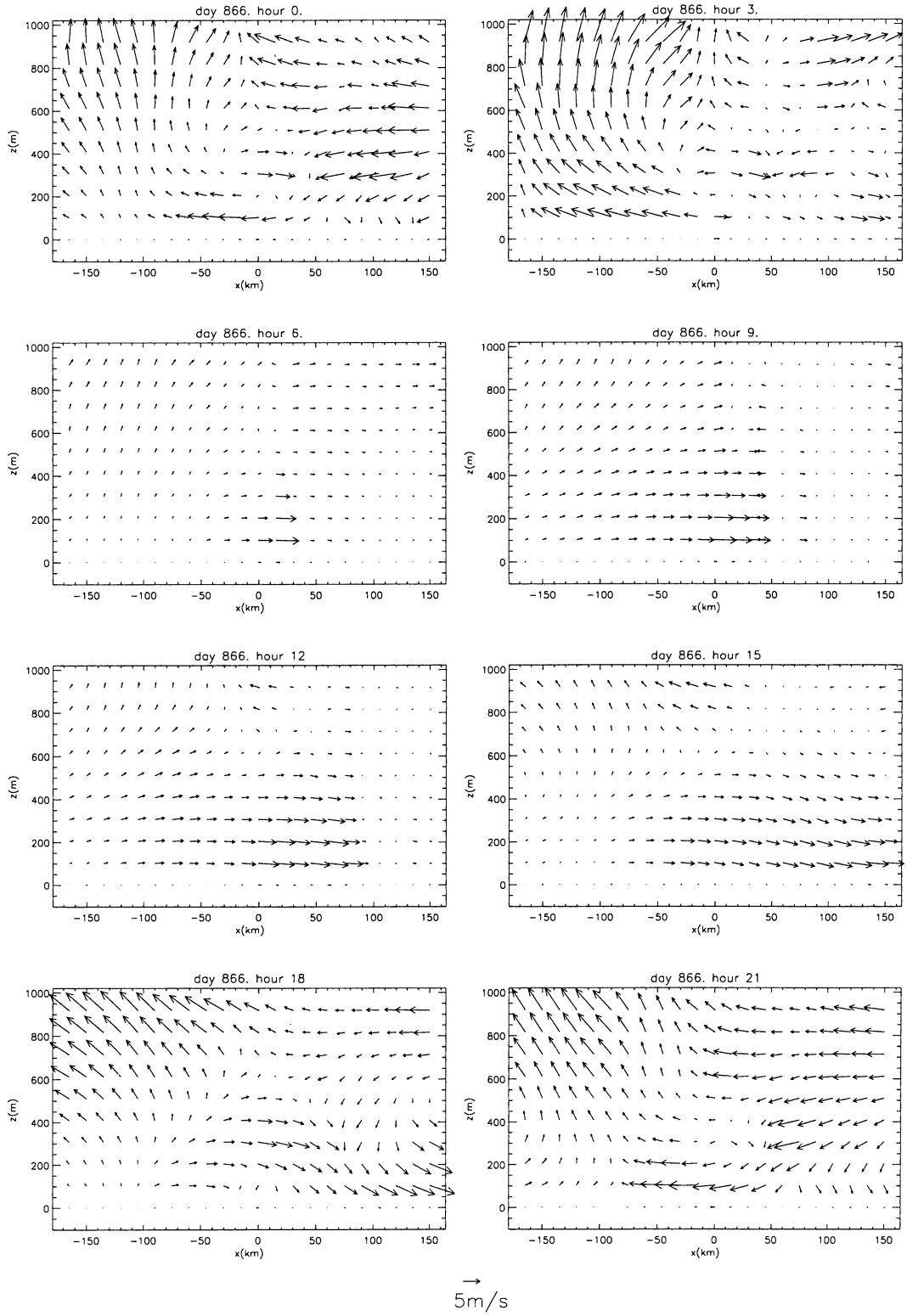

FIG. 2. Same notation as Fig. 1, but for day 866.

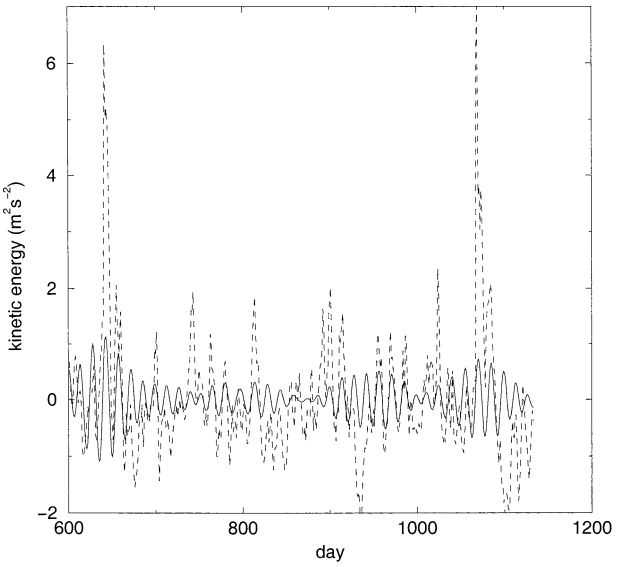

FIG. 3. Time series of average kinetic energy: Eq. (14) (24-h average) minus its mean between days 600–1250 (dashed line) and partial reconstruction of the kinetic energy based on EOFs (4, 5), which has period of 15 days (solid line).

at day 866 is more localized; the inland penetration of the sea-breeze front is slower from 12h to 18h. At 18h, the night of day 641 the land breeze is observed near the coast and later expands inland and toward the sea. In the course of day 866 the land breeze is not observed at 18h.

The change in the circulation from day to day is usually small, thus examining a small part of the time series might give the impression that the solution is periodic with the period of the forcing. When a long time series is considered the solution is found to be nonperiodic, resulting in a dramatic changes such as observed between days 641 and 866.

We begin our analysis by examining the average (over the integration domain) kinetic energy

$$\mathrm{Ke}(t) = \int (u^2 + v^2)\, dx\, dz \Big/ \int dx\, dz \qquad (14)$$

shown in Fig. 3 for the last 625 days. Spells of high and low energy are prominent; for example, day 641 (Fig. 1) belongs to a period of high energy, and day 866 (Fig. 2) belongs to period of moderate energy. In Fig. 4, the power spectrum (PS) of the kinetic energy is shown for $\theta_0 = 14$°C. The most prominent peaks have the periods of 24h, the period of the forcing, and 22.5h. The period 22.5h is the slightly modified inertial oscillation at 32°N. Additional isolated peaks belong to VLFO of 15 and 7 days.

In order to find the role of the different oscillations in the kinetic energy we reconstruct the prominent oscillations by a singular-spectrum analysis (SSA) method (Ghil et al. 2002). To analyze the VLFO we first filter the high frequencies from the time series by applying a 24-h average to the original wind field, so the time lag between two adjacent points in the filtered series is 24 h. Between days 600–1250, 650 sample points were used. The window length (wl) was 60 sample points, that is, 60 days. We examined the robustness of the results by taking wl = 50 sample points and no significant differences were obtained. The prominent oscillation has a period of 15 days and is captured by the reconstructed component (RC) pair (5, 6) explaining 12% of the variance and is shown in Fig. 3. This oscillation is the linear combination of the 24 h and the inertial oscillation; see further discussion below.

In order to analyze the oscillation with a period shorter than 24h we apply a 1-h average filter to the original wind field so the time lag between adjacent points in the filtered series is 1 h. Between days 600–650, 15 600 sample points were used. We used a window length of 120 sample points, that is, of 120 h = 5 days. The 22.4h oscillation, that is, the inertial oscillation, is captured by the RC pair (1, 2) explaining 79% of the variance. This oscillation is prominent at all times except in the time interval between days 802–806, 824–828, etc. Most of the time, the fluctuations of the kinetic energy are in phase with this oscillation (see Fig. 5a).

The 24h oscillation is captured by the RC pair (4, 5) and explains 6% of the variance. The amplitude of this oscillation changes significantly with time. In Fig. 5b, the RC 24h oscillation is shown at the same time interval as in Fig. 5a. When the 24h oscillation is in phase with the fluctuations of the kinetic energy (and so with the 22.4h oscillation), higher values of the kinetic energy are observed, compared to a time interval when the two are out of phase. The time interval between spells of high (low) energy is about 15 days, due to the phase difference between the 22.4h and 24h oscillations, indeed 15 days $= 2\pi/(f_1 - \omega)$ (where $f_1 = 2\pi/22.4$h is the slightly modified inertial oscillation).

Following Plaut and Vautard (1994), Kimoto and Ghil (1993), and Ghil et al. (2002), we define the ghost limit cycle in the phase space as periodic orbits, which are slightly unstable but are visited again and again by the system's trajectories. These ghost limit cycles from the robust skeleton of the attractor. In the breeze simulation, the ghost limit cycle of 24h, 22.4h oscillations together with the ghost limit cycle of the 15-day oscillation form the robust skeleton of the attractor. In the spells when large fluctuations are observed in the kinetic energy, the trajectories in the phase space are captured near the ghost limit cycles of the VLFO, and in the spells when the energy is low, the trajectories are ejected away from these ghost limit cycles.

In order to find the spatiotemporal structure of the ghost limit cycles from the wind field, we applied a multichannel singular-spectrum analysis (M-SSA) method (Plaut and Vautard 1994; Moron et al. 1998; Ghil et al. 2002). In order to keep the size of the matrices that need to be diagonalized manageable, we used a partial domain (between −150 km in sea to 150 km

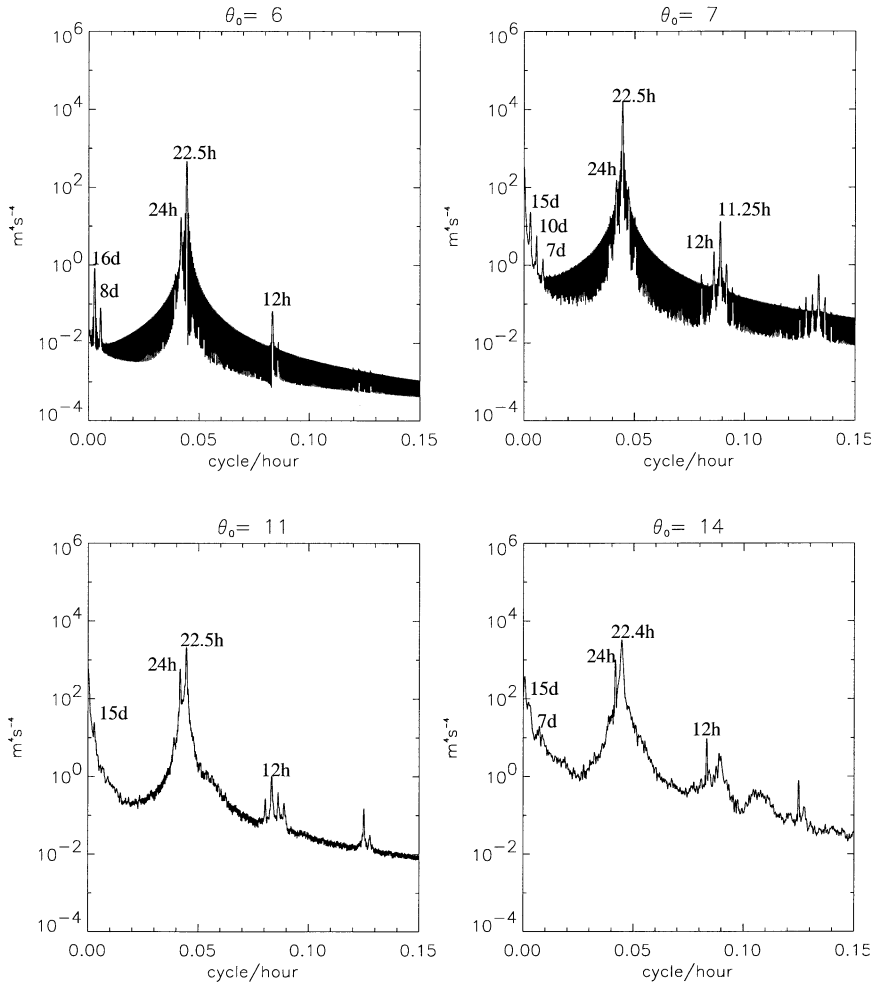

FIG. 4. Power spectrum of kinetic energy for different amplitude of forcing. Period of prominent peaks is also shown (h stands for hours, d is for days).

inland) and only every second grid point along the x axis was taken, though along the z axis, all the points were included. This yields 33×18 grid points for the wind vector (u, v) ($33 \times 18 \times 2$ points), which were used in obtaining the spatial empirical orthogonal functions (S-EOFs) of the wind field.

For the analysis of the 24h and 22.4h oscillations the time series of the wind field (of 720 sample points = 720 h = 30 days) between days 700–730 were used. In these days the 24h and 22.4h oscillations have a significant amplitude (see Fig. 5).

In our analysis, we used the leading 10 S-EOFs that contain 98.9% of the total variance, and a window width of 72 sample points = 72 h. The average cycle of each oscillation we detected was calculated in eight phases according to the phase-compositing technique of Moron et al. (1998). These average cycles are approximation to the ghost limit cycles that form the robust skeleton of the attractor of the breeze.

The mean wind field over the 30 days is shown in Fig. 6a. In the lower levels below 400 m, over the land, a north-northwest wind is observed. Over the sea in the levels above 300 m, a southerly wind is observed, reaching its maximum speed at 130 km over the sea (Fig. 6a). The mean wind field over the last 650 days is very similar to the 30-day mean. In Fig. 6b this mean in the last 650 days is shown over the whole domain. The strong southerly wind is prominent over the sea between the coast and 200 km over the sea at altitudes between 500–3000 m.

The slightly modified inertial oscillation, which has a period of 22.4 h, is captured by the RC pair (3, 4) explaining 44% of the variance. Figure 7 depicts the average composite oscillation in the wind field (u, v) as reconstructed from this pair in eight phases. The stronger winds are observed over the sea in the layers between 1500–2000 m and over the land between 1500–3000 m. The wind rotates in a clockwise direction, with a different rotation rate. The maximum rotation rate is found between phases 5.5h–8.2h and 16.5h–19.2h, when the flow is weakest, and the minimum rate is observed between 11h–13.7h and 22h–2.75h, when the

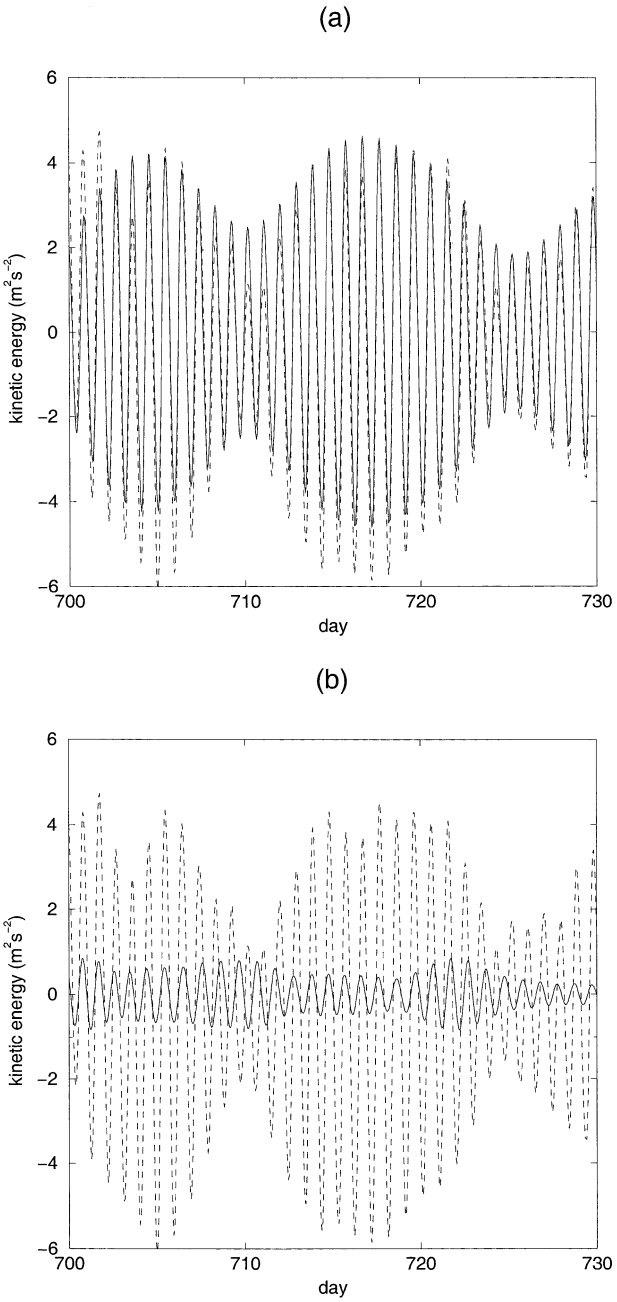

FIG. 5. (a) Same notation as in Fig. 3, but for days 700–730 (solid line) and partial reconstruction of the kinetic energy based on EOFs (1, 2), which has a period of 22.4 h (dashed line). (b) Same as in (a), but with partial reconstruction based on EOFs (4, 5), which has period of 24 h.

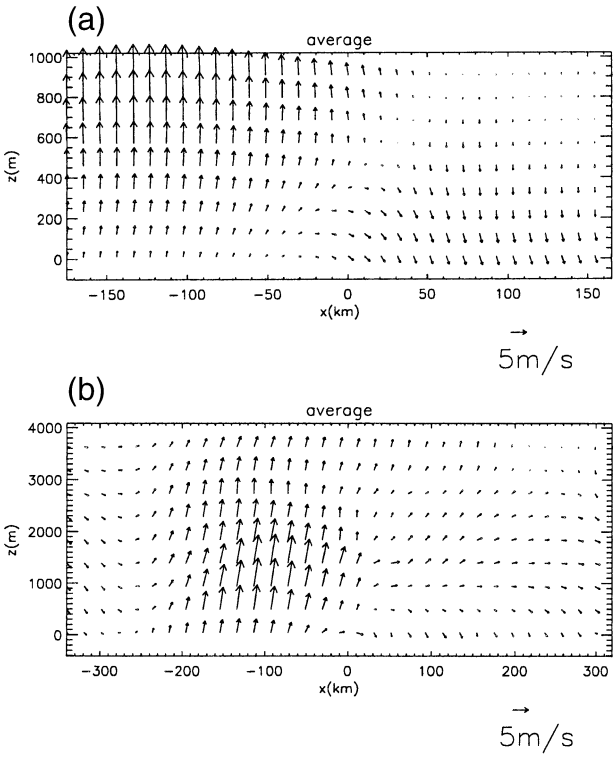

FIG. 6. Mean horizontal wind field (a) in a partial domain (between −150 km to sea and 150 km inland) between days 700–730, and (b) in the whole domain between days 600–1250. Cross section and arrows use the same notation as Fig. 1.

flow is strongest. Since the period of this oscillation is different from the diurnal period, there are days when this oscillation is in phase with the breeze resulting in a large amplitude of the 15-day oscillation and days when these oscillations are out phase and damp the amplitude of 15 days (see also Fig. 5). The 22.4h oscillation has very small amplitude in the lower levels and cannot be detected in observations. The physical reason for this small amplitude in the lower levels is lack of direct forcing of this oscillation and strong friction with the solid boundary below.

The 24h oscillation is captured by the RC pair (1, 2) and explains 44% of the variance. In Fig. 8 we show the average composite oscillation in the wind field (u, v) as reconstructed from this pair in eight phases. Since the oscillation's period is 24 h, we can correspond between the phases and the time of the day. So phase t = 3h corresponds to daily hours 1700–2000 LT, and phase t = 6h corresponds to daily hours 2000–2300 LT, etc. In phases (15h–24h) in the lower layers, a westward wind first develops at the coast and spreads inland and into the sea. This wind can be considered as pure sea breeze, which developed during the daytime in the lower layers (Figs. 1 and 2, 6h–15h). The stronger wind and larger penetration are observed over land. In the upper layers above 1000 m (not shown), a weak return current is observed. The return current is stronger over the land than over the sea. In phases 3h–12h, the land breeze is prominent in the lower levels.

The 24h oscillation is prominent in the region where the 22.4h oscillation is weak, that is, near the coast in the lower levels. This explains why in observations of the wind near the coast in the lower levels the modified inertial oscillation was not observed.

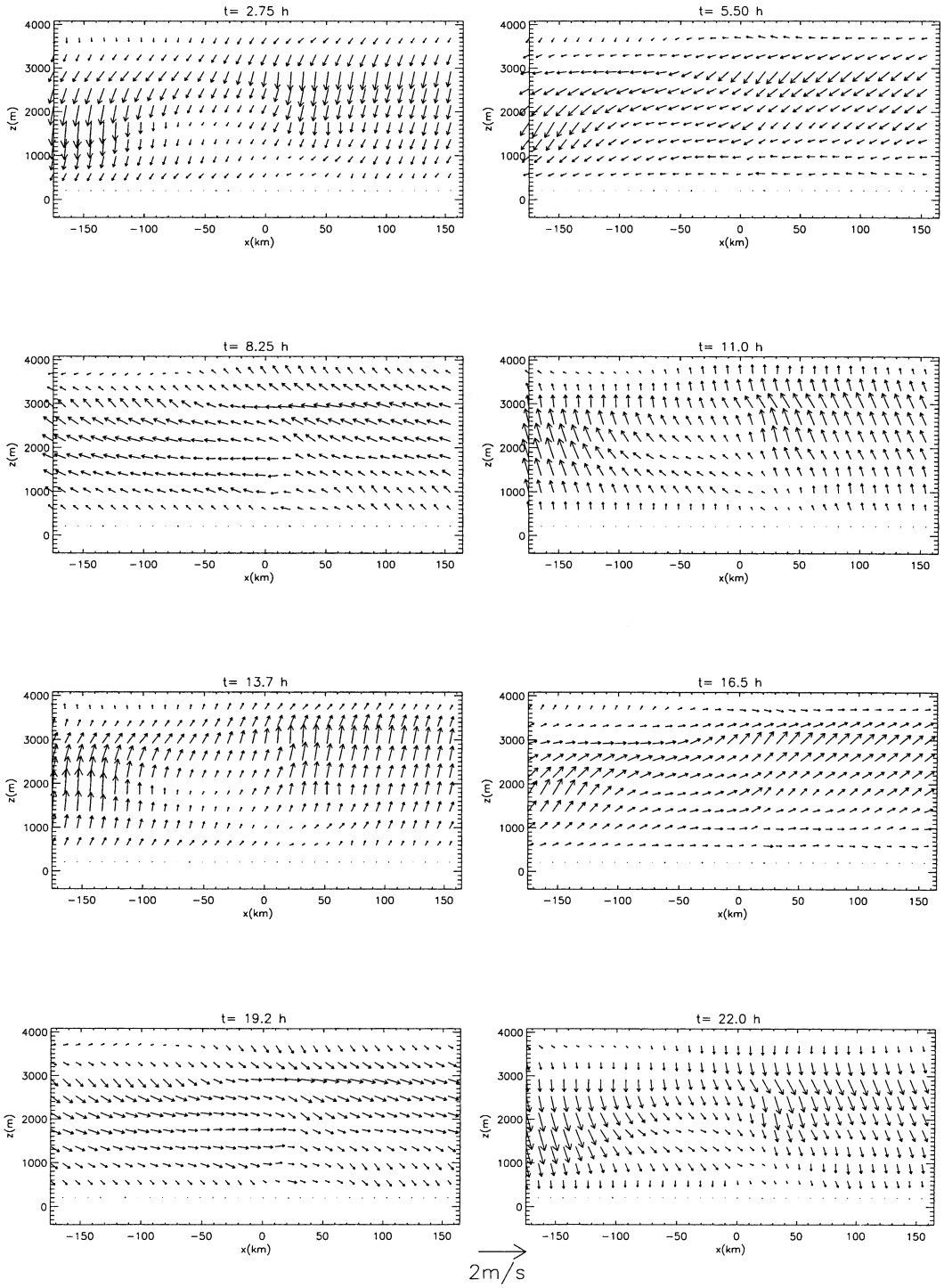

FIG. 7. Average composite 22h oscillation in wind field in a partial domain (between −150 km to sea and 150 km inland) as reconstructed from the pair (3, 4) of ST-EOF and plotted at eight equidistant phases. Phase 1 is in the upper-left panel. Same notation as in Fig. 1.

The 12-h oscillation is captured by the RC pair (5, 6) and explains 3.6% of the variance. In Fig. 9, we show the average composite oscillation in wind field (u, v) as reconstructed from this pair in eight phases (1.5h–12h). This oscillation is significant only over the land and propagates eastward. Since the oscillation's period is 12 h, we can correspond between the phases and the time of the day. So phase $t = 1.5$h corresponds to 1300 (and

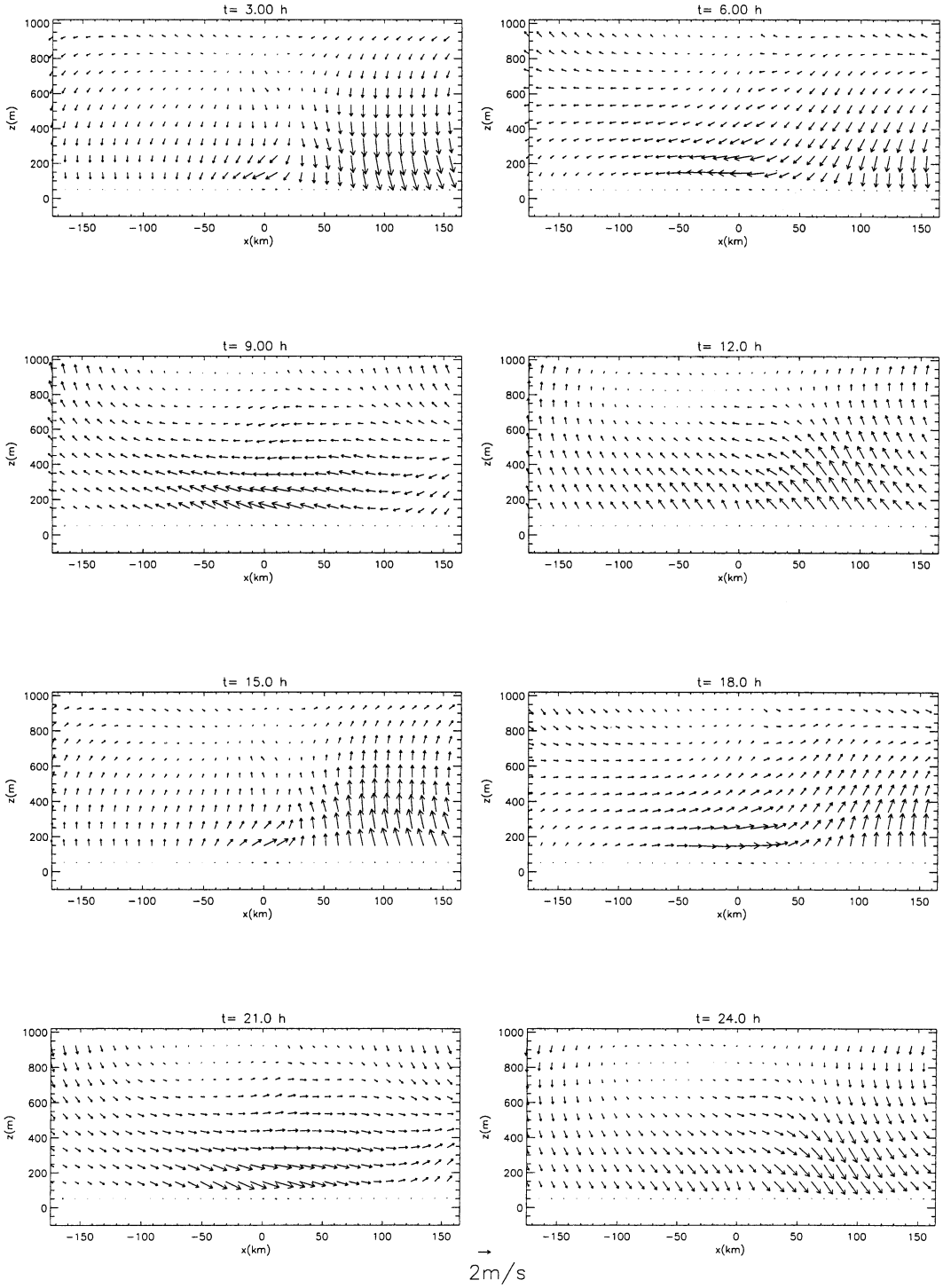

FIG. 8. Same as Fig. 7, but for 24h oscillation as reconstructed from pair (1, 2).

0000) LT, phase $t = 3$h corresponds to 1500 (and 0100) LT, phase $t = 4.5$h corresponds to 1600 (and 0200) LT, etc.

During daytime the 12h oscillation forms the sea breeze front. In phase 7.5h, 20 km inland, the flows converge in the lower layers and diverge in the upper layers. The convergence line propagates eastward. The speed of propagation in phases 7.5h–110.5h is 7 km h^{-1}, and increases to 25 km h^{-1} in phases 12h–3h. Overlapping the phases of these oscillations over the corresponding (with respect to the time of the day) phases in the 24h oscillation shows this tendency. So change

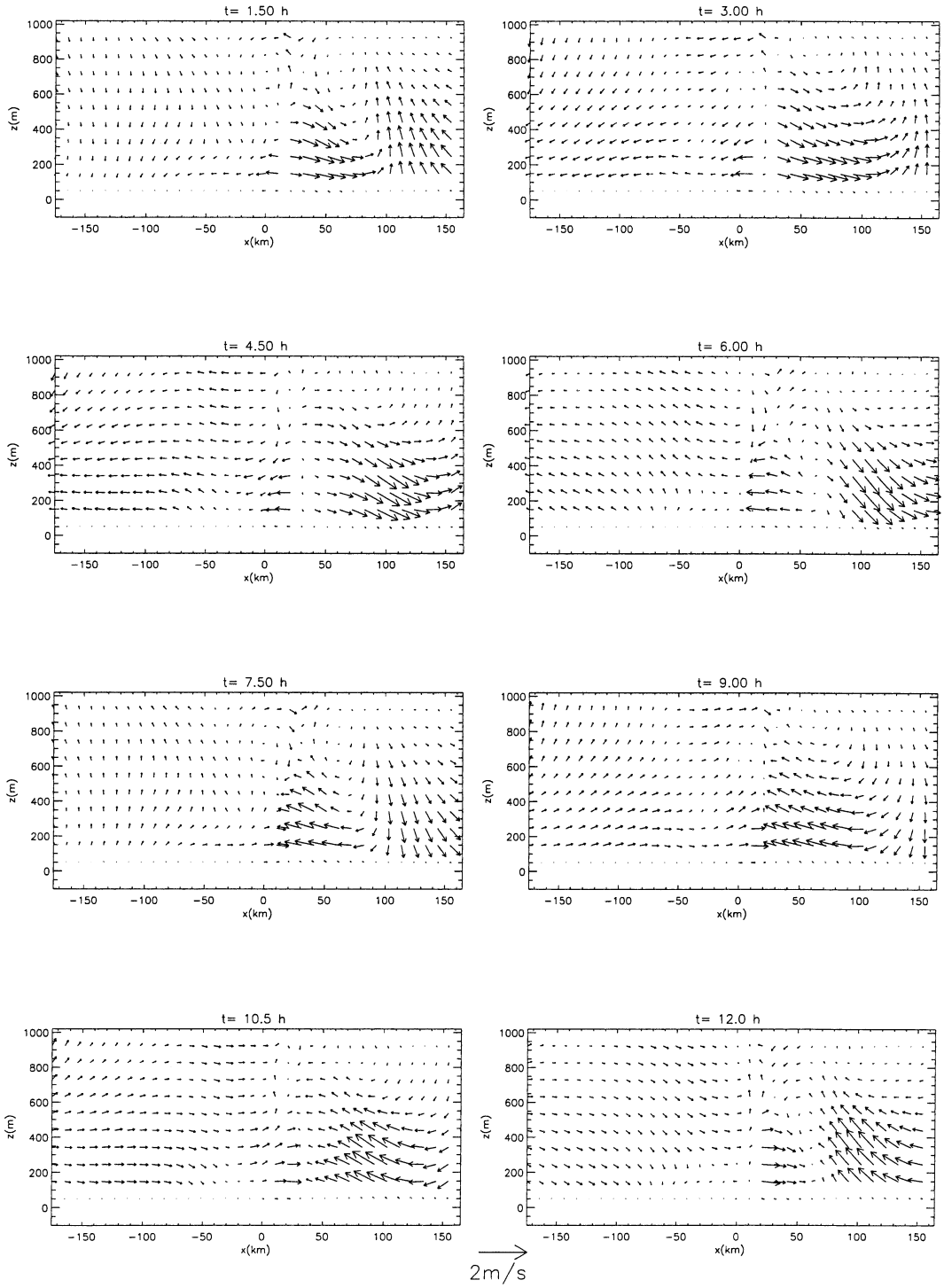

FIG. 9. Same as Fig. 7, but for 12h oscillation as reconstructed from pair (5, 6).

in the propagation speed of the convergence zone corresponds to change in the propagation speed of the seabreeze front, which is slower during the day and faster during the night. Probably the different speed is due to a change in the stability of the atmosphere and to the decrease of the friction with the ground at night (Physik 1976).

During the night, the 12h oscillation tends to advance the land breeze inland, as can be seen by examining the divergence zone. In phase 3h (0100 LT) in the lower

layers, this zone is found 20 km inland. West of this zone eastward flow is observed, which tends to strengthen the land breeze. East of this zone westward flow is observed, which tends to limit the land breeze. Overlapping this oscillation over the corresponding phase (21h) in the 24h oscillation (Fig. 8) shows this tendency. This divergence zone propagates inland as the land breeze expands eastward.

To analyze the VLFO, we first filter the high frequencies from the time series by applying a 24-h average to the original wind field, so the time lag between two adjacent points in the filtered series is 24 h. Between days 600–1250, 650 sample points were used. In our M-SSA analysis we used the leading 10 S-EOFs, which contain 98% of the total variance, and the window length was 60 sample points, that is, 60 days.

The 15-day oscillation is captured by the RC pair (3, 4) and explains 16% of the variance. In Fig. 10, we show the average composite oscillation in u, v as reconstructed from this pair in eight phases (1.87h–15h). The flow's direction is almost independent of the altitude but depends on the location along the x axis. In phases 1.87d–7.52d, the flow in the center of the domain is from the south, and in the other phases it is from the north. The flow is most prominent between -70 and 30 km. In phases 11.2d–13.1d, the northern wind is at its maximum speed, and in phase 3.75d–5.6d, the southern wind is at its maximum speed. The flow in this oscillation is mainly in geostrophic balance. In our two-dimensional domain, the pressure gradient can be only along the x axis so the geostrophic flow must be along the y axis. The structure of this anomaly and its dynamics cannot be reproduced correctly in a two-dimensional domain, so it can change significantly in case of a three-dimensional domain. This is left for further study. The period of this oscillation is a linear combination of the two oscillations $2\pi/f_1 - \omega$, where f_1 is the slightly modified inertial oscillation.

In our model the forcing has a period of 24 h, and thus all the other oscillations found in the simulations are self-sustained. In some models of the breeze (Neumann and Mahrer 1971; Alpert et al. 1982), the 12h and 8h oscillations are added to the forcing. Our results suggest that these oscillations result from nonlinear dynamics.

4. The transition to chaos

In the last section we described in length the breeze for the case where $\theta_0 = 14$°C. The solution was chaotic since it is nonperiodic, as shown from the time series of the kinetic energy (see Fig. 3) and the broadband noise in its power spectrum (see Fig. 4). In this section, we study the transition to chaos as a function of θ_0, the amplitude of the forcing.

The transition to chaos can be examined in a two-dimensional phase plan as the result of the Poincare–Bendixson theorem and the Ruelle–Takens–Newhouse theorem. From the Poincare–Bendixson theorem, chaos cannot occur in a two-dimensional phase plane (Strogatz 2000). On the other hand, following Ruelle–Takens–Newhouse, after three Hopf bifurcations, regular motions become highly unstable in favor of chaotic motion on a strange attractor; that is, the breaking up of the two-dimensional torus (due to the third Hopf bifurcation) results in chaotic solution (Schuster 1995). The two-dimensional torus section appears as a closed curve on the two-dimensional Poincare plan, while a higher torus dimension appears as a complicated curve crossing itself on such a plan. From the time series of the kinetic energy Ke(t) [Eq. (14)], we reconstruct the two-dimensional phase space using the embedding idea (Sauer et al. 1991); that is, the reconstructed two-dimensional phase space is Ke(t), Ke($t + \tau$), where $\tau = 24$ h, that is, the period of the forcing in the breeze case. In Fig. 11, the reconstructed phase space for different θ_0 is shown.

For $\theta_0 \leq 6$°C, the solution is quasi-periodic due to the two incommensurate oscillations, the scillation of the forcing of 24h, and the inertial oscillation, which has a period of $2\pi/f = 22.6$h, where f is the inertial frequency at latitude 32°N. The quasiperiodicity of the solution is shown by the closed curves in the two-dimensional reconstructed phase space (Fig. 11). The average time required to complete a cycle on the closed curve is $2\pi/(f - \omega) = 16$ days. In the power spectrum, Fig. 4, the two incommensurate oscillations, 24h and the inertial oscillation, are prominent. The spatial structures of the 24h and 22.6h oscillations are found by applying the M-SSA analysis to the time series of the wind field with the same parameters as in the previous section. The 24h oscillation was captured by the RC pair (1, 2) and explains 80% of the variance. Figure 12 depicts the average composite oscillation in the wind field (u, v) as reconstructed from this pair in eight phases. This oscillation is limited to the lower atmosphere and to the coastal region, and has a structure similar to the 24h oscillation of the previous section (Fig. 7), but with smaller horizontal and vertical extent. The inertial oscillation 22.6h was captured by the RC pair (3, 4) and explains 8% of the variance. Figure 13 depicts the average composite oscillation in the wind field (u, v) as reconstructed from this pair in eight phases. This oscillation is prominent in the upper layers and over the sea where the 24h oscillation is weak. The structure of this oscillation is similar to the modified inertial oscillation (22.4h) of the previous section.

Another prominent oscillation whose period is 16 days is obtained in the power spectrum. This oscillation is a linear combination of the two incommensurate frequencies; that is, $2\pi/(f - \omega) = 16$ days. It is in geostrophic balance and resembles the VLFO of the previous section.

By increasing the forcing to $\theta_0 = 7$°C, the solution becomes aperiodic, as shown by the distribution of points in the reconstructed phase space, which does not lie on the closed curve (Fig. 11). In the power spectrum

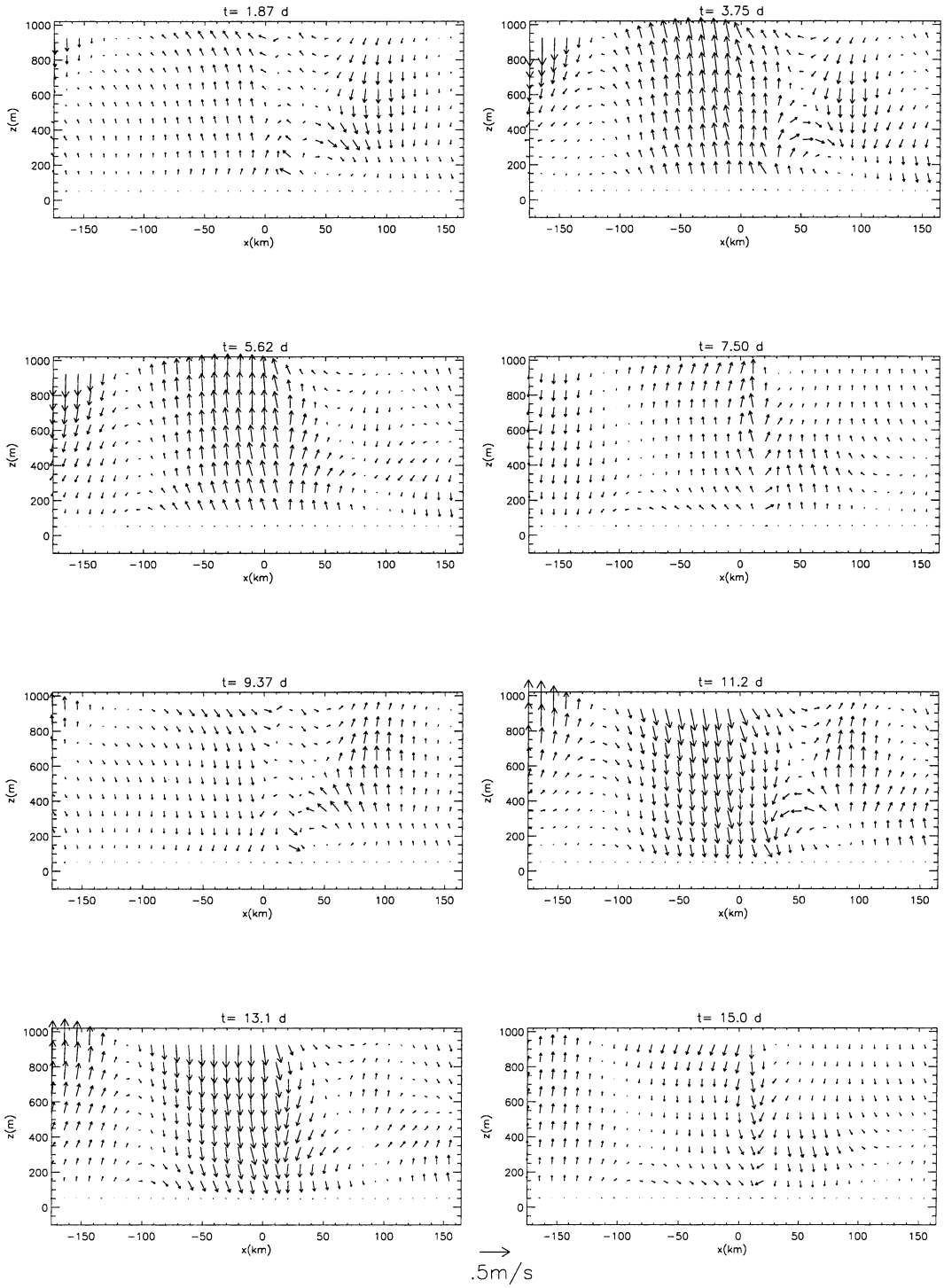

FIG. 10. Same as Fig. 7, but for VLFO as obtained from filtered time series; 15-day oscillation was reconstructed from pair (3, 4) of the ST-EOF.

(Fig. 4) the significant peaks have periods of 24h, 22.5h, their harmonics, and the VLFO of 15d, 10d, and 7d. The energy in the other frequencies are larger by an order of magnitude compared to $\theta_0 = 6°C$.

By increasing the forcing to $\theta_0 = 10°C$, a chaotic solution is obtained, as can be seen in the reconstructed phase space by the broad distribution of the points (Fig. 11). The structure of the points' distribution resembles the closed curve of the a periodic solution obtained for $\theta_0 = 7°C$ with a larger energy value.

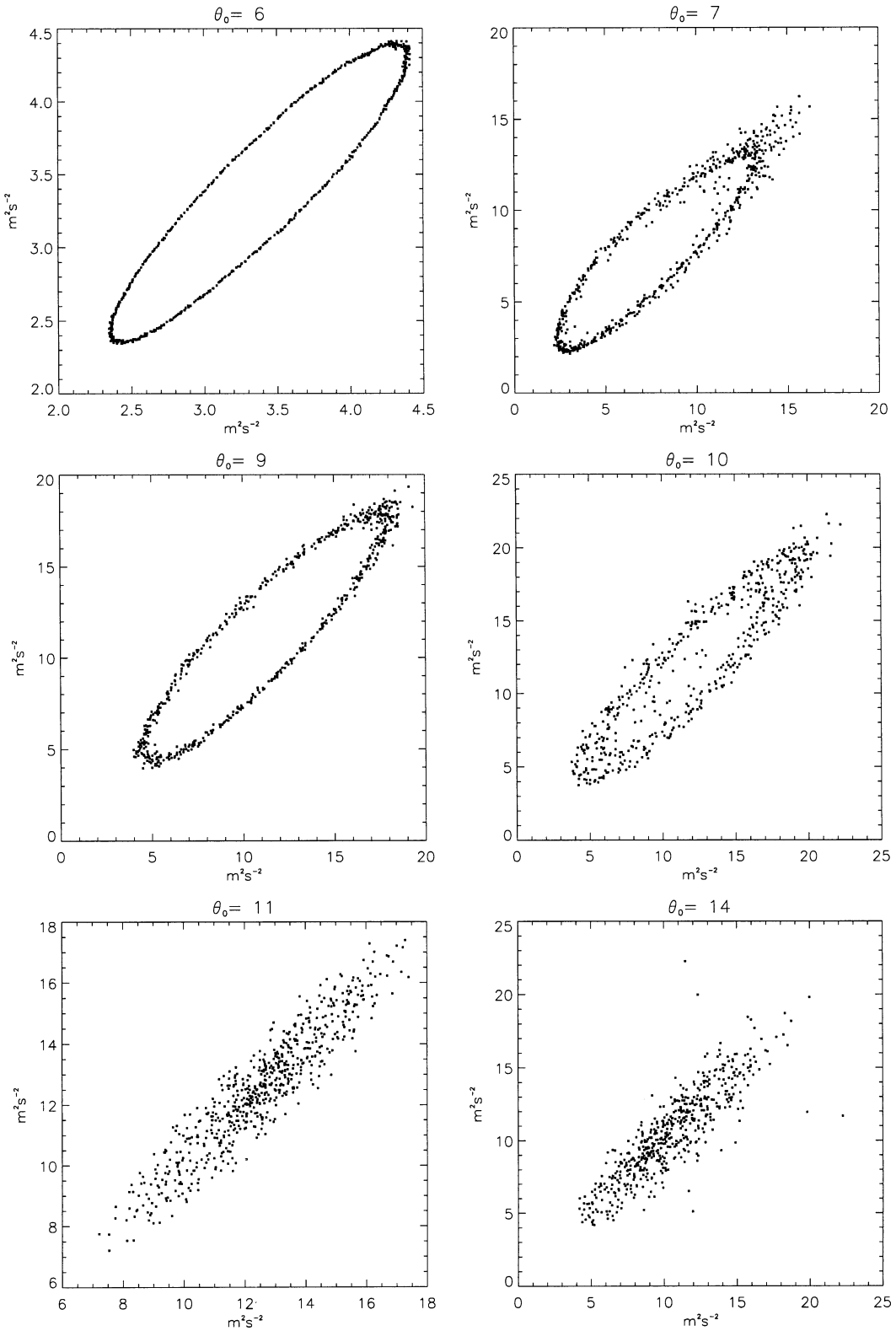

FIG. 11. Reconstructed two-dimensional phase space from time series of kinetic energy [Ke(t), Ke($t + \tau$)]; $\tau = 24$ h.

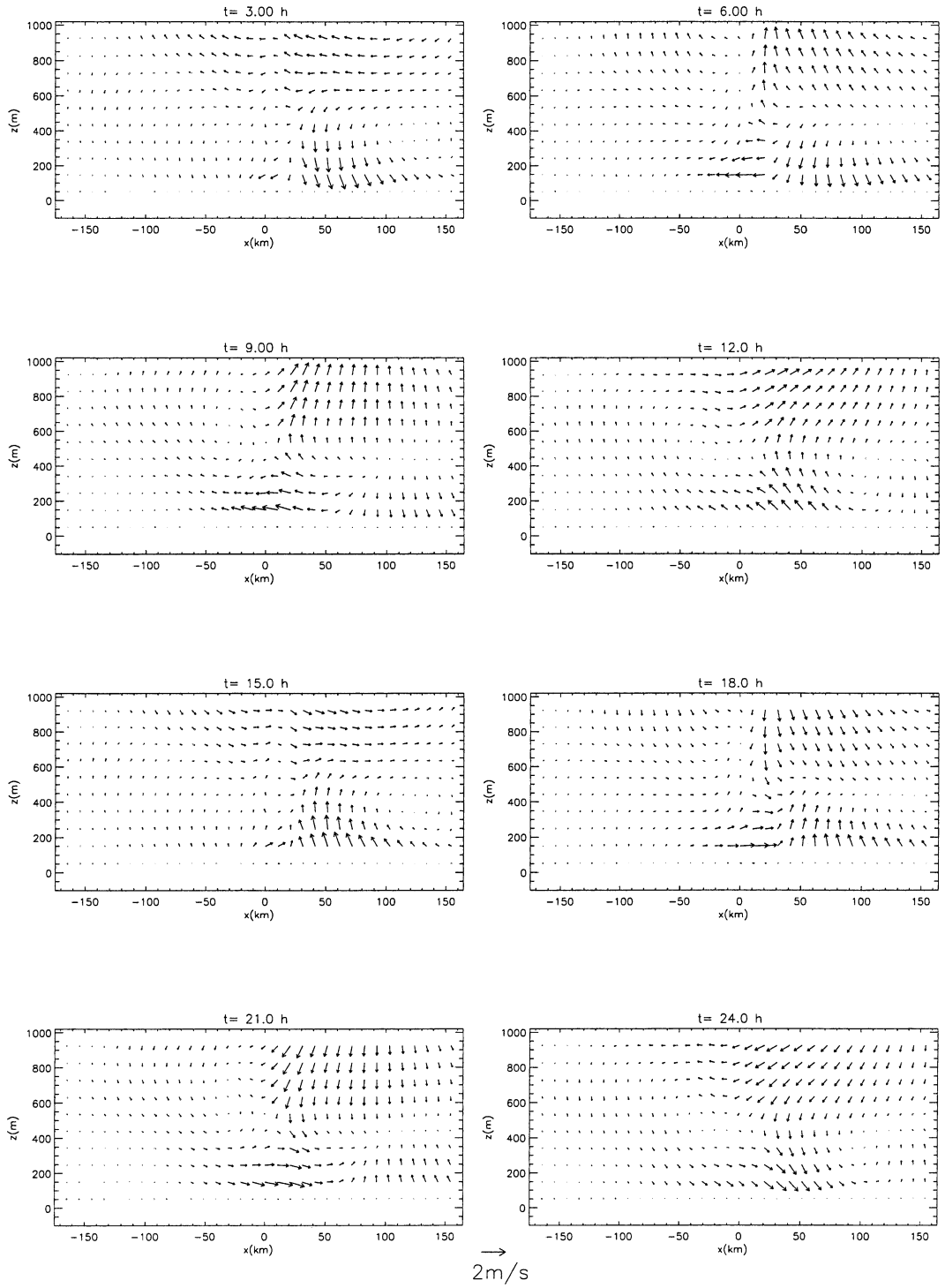

FIG. 12. Same as Fig. 7, but for the case $\theta_0 = 6$°C and 24h oscillation as reconstructed from the pair (1, 2).

Further increasing the forcing to $\theta_0 = 11$°C causes the points in the reconstructed phase space to become densely distributed. In the power spectrum (Fig. 4), broadband noise is observed. Similar qualitative chaotic solution is obtained for $\theta_0 = 14$°C, as shown in the phase space (Fig. 11), and in the power spectrum (not shown) the prominent peaks are almost the same. This case was investigated thoroughly in the previous section.

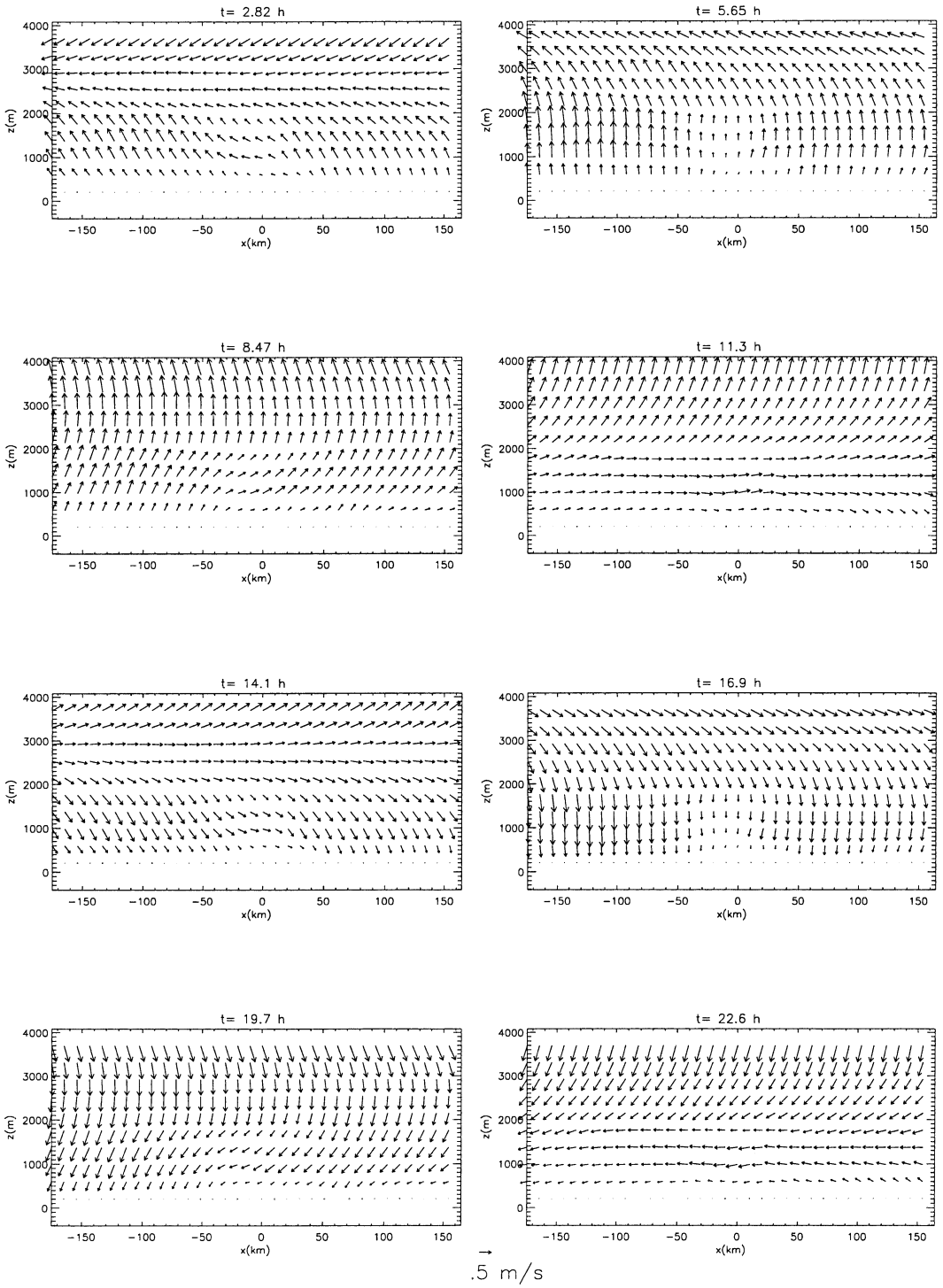

FIG. 13. Same as Fig. 7, but for the case $\theta_0 = 6°C$ and 22.6h oscillation as reconstructed from the pair (3, 4).

5. Observation of the breeze

Most of the long records (several months) of the breeze are limited to measurement stations usually 10 m above the ground and so cannot capture the oscillations that are prominent in the high altitudes found in this numerical study, such as the inertial oscillation. However, some oscillations can be captured by low-level measurements like the 24h oscillation and its harmonics and the VLFO.

In this section we analyze observation of the horizontal wind from mid-May to mid-October 1999

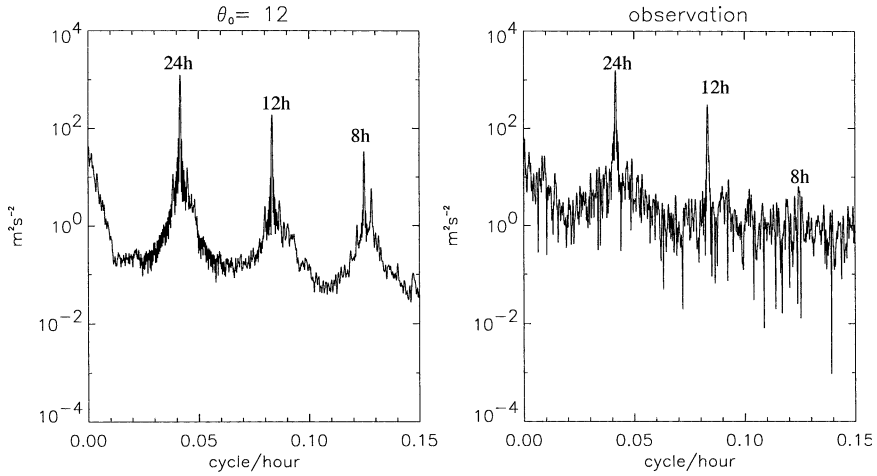

FIG. 14. Power spectrum of wind speed in observation and in model simulation.

(170 days) in the central coast of Israel about 2.5 km inland and 60 m above the ground.

The synoptic system present in most of the summer months over Israel (June–September) near the surface is a warm trough, which is an extension of the Indian monsoon low. Under these conditions the sea and land breeze is the most prominent surface wind along the Mediterranean coast of Israel.

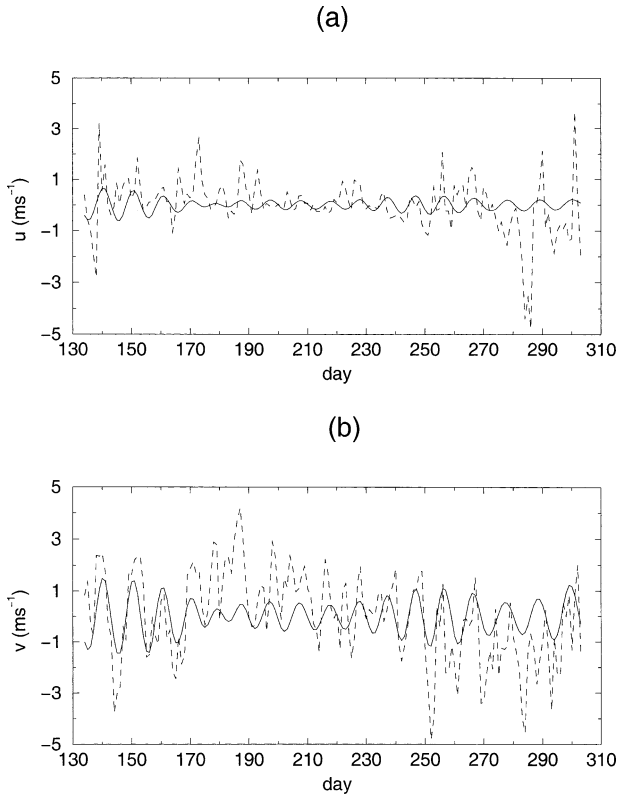

FIG. 15. Time series of daily mean wind components during summer (solid line), the partial reconstruction of the wind based on EOFs (2, 3), which has a period of 10 days (dashed line); u is the east–west component and v is the north–south component.

In Fig. 14, the PS of the observed wind speed is shown. Also, the PS of the model solution with forcing of $\theta_0 = 12°C$, 2.5 km inland, 80 m above the ground (model level) is shown. The prominent peaks have periods of 24h and 12h, and the power of these peaks is about the same in observation and simulation. The broadband noise found in the whole spectrum indicates the chaotic character of the wind. The inertial oscillation is not observed in the power spectrum, and in the simulation this oscillation is prominent only in the upper layers (Figs. 7 and 13). We assume that this is also the case in observations; that is, the inertial oscillation is prominent at altitudes of several hundred meters and is not detected in observations near the ground.

In order to examine the VLFO in the observations, we first filter from the observations the oscillations whose periods are shorter than 24 h by taking the daily mean of the series. The filtered wind vector is shown in Fig. 15. To find the prominent oscillations we perform M-SSA analysis on the filtered wind vector so the number of channels in this case is 2, the wl = 30, sample points = 30 days. The most energetic oscillation has a period of 10 days and is captured by the reconstructed component pair (2, 3) and explains 15% of the variance. In Fig. 15, the partial RC wind components based on the pair (2, 3) are shown. The 10-day oscillation is prominent in the v component; this component is parallel to the central coast of Israel. A Monte Carlo SSA significance test was performed on the v component of the average wind (Ghil et al. 2002). The eigenvalue of the 10-day oscillation was above the 95% noise percentile; that is, the red noise hypothesis for the associate EOF and PC can be rejected with 95% level of significance. We interpret this VLFO as the result of the nonlinear dynamics interaction between the inertial oscillation (period of 21.8h) at central latitude of the eastern Med-

iterranean, 33.5°N, and the 24h oscillation. In the model in the chaotic regime, we obtained such an oscillation whose period was 15 days due to different central latitude of the model. The flow in the VLFO oscillations is parallel to the coast (Fig. 10), which strengthens the assumption that the observed 10-day oscillation corresponds to the VLFO of our model.

The analysis here is preliminary, and more extensive studies are needed to establish the relation between VLFO and the breeze.

6. Summary

In this work we studied the evolution of the sea and land breeze by a nonlinear model under calm synoptic conditions and diurnal periodic forcing of the ground temperature. The breeze was examined as a function of the strength of the amplitude of the ground temperature θ_0. For $\theta_0 \leq 6$°C, the solution is quasi periodic due to the two incommensurate oscillations of 24h and 22.6h (the inertial oscillation at latitude 32°N). The 22.6h oscillation is prominent in the upper layers, while the 24h oscillation is confined to the lower layers. A VLFO of 16 days is the linear combination of the two incommensurate oscillations. This oscillation is in geostrophic balance so the flow is along the north–south axis. Increasing the forcing amplitude to $\theta_0 \geq 7$°C, the solution becomes nonperiodic. Further increasing the forcing to $\theta_0 \geq 10$°C, the solution becomes chaotic. The solution for $\theta_0 = 14$°C is examined in detail. The prominent oscillations can be divided into two classes, where the time scale of one class is 1 day and shorter, such as the 24h, 22.4h, and their harmonics, and the time scale of the other class is larger than a week, such as 15 days. The flow in this class is in geostrophic balance. The 24h oscillation is prominent in the lower layers and can be considered as pure sea and land breeze. Its harmonic oscillation of 12h is significant over the land and forms the sea-breeze front. The 22.4h oscillation is a modified inertial oscillation since its period and spatial structure is close to that of the inertial oscillation obtained for $\theta_0 = 6$°C. This oscillation is prominent in the upper layers and over the sea. It is not easy to find these oscillations in observations since the measurements are usually conducted in the lower layers over the land. The 15d oscillation is a linear combination of the 24h and 22.4h oscillations. Spells of very large kinetic energy are prominent.

In this study, we show that there are significant differences between the nonlinear model and linear models beyond the formation of the sea-breeze front and the propagation of the cold sea air inland. The self-sustained oscillations such as the 12h, 8h, ~22.5h, and the VLFO in the quasi-periodic, nonperiodic, and chaotic solutions are unique to nonlinear models. These oscillations, their spatial structure, and the transition to chaos were not studied in previous nonlinear models.

We assume that the route to chaos found by this model for the breeze is generic to the breeze and does not depend on the parameterization of the vertical exchange eddy coefficient used in this model. Only the regimes where quasi periodic, aperiodic, and chaotic solutions exist can depend on the parameterization of the vertical exchange eddy coefficient. The 2D and 3D turbulence are quite different and since our model is a 2D model, it is possible that the model results are more sensitive to the parameterization of the vertical turbulent eddy coefficient than a 3D model. Previous studies of the breeze by 2D models by Neuman and Mahrer (1971), Alpert et al. (1982), and many others show great similarity between their solutions and observations. So it is reasonable to assume that the parameterization of the turbulence in the 2D model used in these models is reasonable.

In order to relate our analysis to observations of the breeze, we analyzed a long record (170 days) of the wind along the central coast of Israel during the summer. The most prominent wind in this time of the year is the sea and land breeze due to the weak synoptic systems that prevail in that region. The power spectrum of the observed and the computed wind has great similarity. The prominent peaks of 24h and 12h have the same power; the inertial oscillation is missing from both time series since this oscillation is prominent only at altitudes of several hundred meters. In the observations a VLFO of order of 10 days is the most energetic oscillation whose period is larger than 24h. This oscillation is prominent in the alongshore component. We interpret this VLFO as the result of the nonlinear interaction between the inertial oscillation at central latitude of the eastern Mediterranean and the 24h oscillation. In the model as in observations, this oscillation is characterized by its alongshore flow. The analysis here is preliminary, and more extensive studies are needed to establish the relation between VLFO and the breeze; particularly, observations at altitudes of several hundred meters are needed to verify the results of this study.

The study of the route to chaos as a function of latitude and under different synoptic conditions is left for further research. The VLFO found in the model has a time scale much larger than the synoptic systems. It is interesting to examine these oscillations in three-dimensional models since the flow is symmetric with respect to the y axis (parallel to the coast). Breaking of symmetry due to bifurcation of the solution might result in a three-dimensional complex flow. The flow in the VLFOs found here are equivalent barotropic and in geostrophic balance. Their dynamics are mainly in the horizontal and so cannot be resolved by a two-dimensional vertical cross section. We note that the synoptic systems during the summer in the eastern Mediterranean are very weak, so such oscillations can survive.

Acknowledgments. I am grateful to Dr. Yael Radzyner for the careful reading of this manuscript.

REFERENCES

Alpert, P., A. Cohen, J. Neuman, and E. Doron, 1982: A model simulation of the summer circulation from the eastern Mediterranean past Lake Kinneret in the Jordan Valley. *Mon. Wea. Rev.,* **110,** 994–1006.

——, M. Kusuda, and N. Abe, 1984: Anticlockwise rotation, eccentricity and tilt angle of the wind hodograph. Part II: An observational study. *J. Atmos. Sci.,* **41,** 3558–3573.

Atkinson, B. W., 1989: *Meso-Scale Atmospheric Circulations.* Academic Press, 495 pp.

Dalu, G. A., and R. A. Pielke, 1989: An analytical study of the sea breeze. *J. Atmos. Sci.,* **46,** 1815–1825.

Estoque, M. A., 1961: A theoretical investigation of the sea breeze. *Quart. J. Roy. Meteor. Soc.,* **87,** 136–146.

Feliks, Y., 1988: The sea-breeze front analytical model. *J. Atmos. Sci.,* **45,** 1030–1038.

——, 1993: A numerical model for estimation of the diurnal fluctuation of the inversion height due to a sea breeze. *Bound.-Layer Meteor.,* **62,** 151–161.

——, 2000: An analytical model of gravity currents in a stable atmosphere. *J. Fluid Mech.,* **420,** 27–46.

Fletcher, C. A. J., 1991: *Computational Techniques for Fluid Dynamics.* Vol. 1. 2d ed. Springer, 401 pp.

Ghil, M., and Coauthors, 2002: Advanced spectral methods for climatic time series. *Rev. Geophys.,* **40,** 1–41.

Haurwitz, B., 1947: Comments on the sea-breeze circulation. *J. Meteor.,* **4,** 1–8.

Huss, A., and Y. Feliks, 1981: A mesometeorological numerical model of the sea and land breezes involving sea–atmospheric interactions. *Beitr. Phys. Atmos.,* **34,** 238–257.

Kimoto, M., and M. Ghil, 1993: Multiple flow regimes in the Northern Hemisphere winter. Part II: Sectorial regimes and preferred transitions. *J. Atmos. Sci.,* **50,** 2645–2673.

Kusuda, M., and P. Alpert, 1983: Anticlockwise rotation of the wind hodograph. Part I: Theoretical study. *J. Atmos. Sci.,* **40,** 487–499.

Lambert, S., 1974: High resolution numerical study of the sea-breeze front. *Atmosphere,* **12,** 97–105.

Lettau, H. H., 1962: Theoretical wind spirals in the boundary layer of barotropic atmosphere. *Beitr. Phys. Atmos.,* **35,** 195–212.

Marchuk, G. I., 1975: *Methods of Numerical Mathematics.* Springer, 316 pp.

Moron, V., R. Vautard, and M. Ghil, 1998: Trends, interdecadal and interannual oscillations in global sea-surface temperatures. *Climate Dyn.,* **14,** 545–568.

Neumann, J., 1977: On the rotation rate of the direction of sea and land breezes. *J. Atmos. Sci.,* **34,** 1913–1917.

——, and Y. Mahrer, 1971: A theoretical study of the land and sea breeze circulation. *J. Atmos. Sci.,* **28,** 532–542.

——, and ——, 1974: Evolution of a sea breeze front; A numerical study. *Bonn Met. Abh.,* **17,** 481–492.

Pandolfo, J. P., and C. A. Jacobes, 1973: Tests on urban meteorological pollutant model using co-validation data in Los Angeles metropolitan area. Center for Environment of Man Rep. 490a, 172 pp.

Pearson, R. A., 1973: Properties of the sea breeze front as shown by numerical model. *J. Atmos. Sci.,* **30,** 1050–1060.

Physik, W., 1976: A numerical model of the sea-breeze phenomenon over a lake or gulf. *J. Atmos. Sci.,* **33,** 2107–2135.

Plaut, G., and R. Vautard, 1994: Spells of low-frequency oscillations and weather regimes in the Northern Hemisphere. *J. Atmos. Sci.,* **51,** 210–236.

Sauer, T., J. A. Yorke, and M. Casdagli, 1991: Embedology. *J. Stat. Phys.,* **65,** 579–616.

Schuster, H. G., 1995: *Deterministic Chaos: An Introduction.* 3d ed. Wiley-VCH, 291 pp.

Strogatz, S. H., 2000: *Nonlinear Dynamics and Chaos.* Westview Press, 498 pp.